Supplement of Atmos. Chem. Phys. Discuss., 14, 24475–24521, 2014
http://www.atmos-chem-phys-discuss.net/14/24475/2014/
doi:10.5194/acpd-14-24475-2014-supplement

Atmospheric Chemistry and Physics
Open Access
Discussions

Supplement of

Influence of satellite-derived photolysis rates and NO_x emissions on Texas ozone modeling

W. Tang et al.

Correspondence to: D. S. Cohan (cohan@rice.edu)

Supplement of

Influence of satellite-derived photolysis rates and NO_x emissions on Texas ozone modeling

1. CAMx modeled profile-based OMI retrieval

The OMI-retrieved tropospheric NO_2 vertical column density (VCD) used in this study is calculated via Eq. (S1) (Bucsela et al., 2013),

$$V_{c(GEOSChem)} = \frac{S_{c(OMI)}}{AMF_{GEOSChem}} \quad \text{(S1)}$$

where $S_{c(OMI)}$ is the OMI tropospheric NO_2 slant column density, *AMF* stands for the air mass factor which is computed based on a priori GEOS-Chem modeled profile and scattering weights (*SW*) calculated by the TOMRAD model (Bucsela et al., 2013), and $V_{c(GEOSChem)}$ is the GEOS-Chem modeled profile-based OMI tropospheric NO_2 VCD. A satellite NO_2 retrieval error analysis study (Boersma et al., 2004) shows that the estimated a priori profile from global models may contribute approximately 10% uncertainty to the AMF calculations and propagate that uncertainty to the retrieved NO_2 VCD. Therefore, when OMI VCD is compared to any modeled VCD, OMI averaging kernels (*AKs*) (Eskes and Boersma, 2003), calculated in Eq. (S2), are recommended to be applied to the modeled VCDs via Eq. (S3), in order to remove the influence from the a priori profile used in the OMI retrievals.

$$AK_i = \frac{SW_i}{AMF_{GEOSChem}} \quad \text{(S2)}$$

$$C_{NO_2}^{predicted} = \sum(AK_i \times CAMx_{vci}) = \sum(\frac{SW_i}{AMF_{GEOSChem}} \times CAMx_{vci}) = \frac{\sum(SW_i \times CAMx_{vci})}{AMF_{GEOSChem}}$$
$$= CAMx_{vctot} \times \frac{\sum(SW_i \times CAMx_{vci}) / CAMx_{vctot}}{AMF_{GEOSChem}} \quad \text{(S3)}$$

In Eq. (S3), $CAMx_{vci}$ represents the CAMx modeled NO_2 VCD at each model layer (*i*), and $CAMx_{vctot}$ is the CAMx modeled total tropospheric VCD. The AMF which contains the a priori GEOS-Chem modeled profile is now merged with the CAMx modeled VCD.

The way of removing the a priori GEOS-Chem modeled profile via applying AKs is carried out by generating the CAMx modeled profile-based AMF_{CAMx} as shown in Eq. (S4),

$$AMF_{CAMx} = \Sigma(SW_i \times \frac{CAMx_{vci}}{CAMx_{vctot}}) = \frac{\Sigma(SW_i \times CAMx_{vci})}{CAMx_{vctot}} \quad \text{(S4)}$$

using AMF_{CAMx} to replace $AMF_{GEOSChem}$ in Eq. (S1) and then creating a CAMx modeled profile-based OMI tropospheric NO_2 VCD ($V_{c(CAMx)}$). However, this procedure can only be realized in the inversion process by comparing the AKs applied CAMx VCD ($C_{NO_2}^{predicted}$) and original OMI retrieved VCD ($V_{c(GEOSChem)}$).

The numerator in Eq. (S3) can be replaced by the AMF_{CAMx} generated in Eq. (S4) to form Eq. (S5).

$$C_{NO_2}^{predicted} = CAMx_{vctot} \times \frac{AMF_{CAMx}}{AMF_{GEOSChem}} \quad \text{(S5)}$$

When applying $C_{NO_2}^{predicted}$ to the direct scaling method (Martin et al., 2003; Tang et al., 2013) in Eq. (S6),

$$E_t = E_b \times \frac{V_{c(GEOSChem)}}{C^{predicted}_{NO_2}} = E_b \times \frac{\dfrac{S_{c(OMI)}}{AMF_{GEOSChem}}}{CAMx_{vctot} \times \dfrac{AMF_{CAMx}}{AMF_{GEOSChem}}} = E_b \times \frac{\dfrac{S_{c(OMI)}}{AMF_{CAMx}}}{CAMx_{vctot}} = E_b \times \frac{V_{c(CAMx)}}{CAMx_{vctot}} \qquad \text{(S6)}$$

the $AMF_{GEOSChem}$ is canceled out, and $V_{c(CAMx)}$is formed through AMF_{CAMx} to compare with the CAMx modeled VCD directly.

When applying OMI AKs to the CAMx modeled NO_2 and its sensitivity VCDs in the DKF method (Tang et al., 2013) as shown in Eq. (S7),

$$\begin{aligned}\hat{\mathbf{x}}_{\mathrm{NO_x}} = \mathbf{x}^{-}_{\mathrm{NO_x}} + \mathbf{P}^{-}_{\mathrm{NO_x}} \times \left(\frac{AMF_{CAMx}}{AMF_{GEOSChem}}\right)\mathbf{S}^{\mathbf{T}}_{vc} \times \left(\left(\frac{AMF_{CAMx}}{AMF_{GEOSChem}}\right)^2 \mathbf{S}_{vc}\mathbf{P}^{-}_{\mathrm{NO_x}}\mathbf{S}^{\mathbf{T}}_{vc} + \left(\frac{S_{c(OMI)}}{AMF_{GEOSChem}}\varepsilon_{OMI}\right)^2\right)^{\mathbf{-1}} \\ \times\left(\left(\frac{S_{c(OMI)}}{AMF_{GEOSChem}}\right) - \left(CAMx_{vctot} \times \frac{AMF_{CAMx}}{AMF_{GEOSChem}}\right) - \left(\frac{AMF_{CAMx}}{AMF_{GEOSChem}}\right)\mathbf{S}_{vc}\mathbf{x}^{-}_{\mathrm{NO_x}}\right)\end{aligned} \qquad \text{(S7)}$$

where ε_{OMI} is the OMI measurement uncertainty, Eq. (S8) derived

$$\begin{aligned}\hat{\mathbf{x}}_{\mathrm{NO_x}} = \mathbf{x}^{-}_{\mathrm{NO_x}} + \mathbf{P}^{-}_{\mathrm{NO_x}} \times \mathbf{S}^{\mathbf{T}}_{vc} \times \left(\mathbf{S}_{vc}\mathbf{P}^{-}_{\mathrm{NO_x}}\mathbf{S}^{\mathbf{T}}_{vc} + \left(\frac{S_{c(OMI)}}{AMF_{CAMx}}\varepsilon_{OMI}\right)^2\right)^{\mathbf{-1}} \\ \times\left(\frac{AMF_{GEOSChem}}{AMF_{CAMx}}\right) \times \left(\frac{S_{c(OMI)}}{AMF_{GEOSChem}} - \left(CAMx_{vctot} \times \frac{AMF_{CAMx}}{AMF_{GEOSChem}}\right) - \left(\frac{AMF_{CAMx}}{AMF_{GEOSChem}}\right)\mathbf{S}_{vc}\mathbf{x}^{-}_{\mathrm{NO_x}}\right)\end{aligned} \qquad \text{(S8)}$$

and further transformed to Eq. (S9),

$$\hat{\mathbf{x}}_{\mathrm{NO_x}} = \mathbf{x}^{-}_{\mathrm{NO_x}} + \mathbf{P}^{-}_{\mathrm{NO_x}} \times \mathbf{S}^{\mathbf{T}}_{vc} \times \left(\mathbf{S}_{vc}\mathbf{P}^{-}_{\mathrm{NO_x}}\mathbf{S}^{\mathbf{T}}_{vc} + (V_{c(CAMx)}\varepsilon_{OMI})^2\right)^{\mathbf{-1}} \times \left(V_{c(CAMx)} - CAMx_{vctot} - \mathbf{S}_{vc}\mathbf{x}^{-}_{\mathrm{NO_x}}\right) \qquad \text{(S9)}$$

where all $AMF_{GEOSChem}$ are removed, and the original $V_{c(GEOSChem)}$ becomes $V_{c(CAMx)}$.

There is an alternative way to create $V_{c(CAMx)}$ instead of applying OMI AKs, which is to use the CAMx modeled profile directly in the OMI retrieval process. In this case, the error of interpolating AKs values into the CAMx layer can be avoided, and the CAMx profile-based OMI retrieval can be calculated directly and viewed. In this study, we have created a CAMx profile-based OMI product that uses a CAMx profile in the retrieval process for the AMF calculation and planned to use this new OMI retrieval product at the beginning for the inversion study. However, we find that the CAMx profile-based OMI overestimates NO_2 VCD by approximately 30% compared to the original OMI retrieval using a GEOS-Chem profile (Fig. S1, right). We further compare the monthly averaged 13:00-14:00LT CAMx NO_2 profile to the GEOS-Chem NO_2 profile over the 12km domain (Fig. S1 left) and find that the CAMx profile shows much higher amounts of NO_2 in the boundary layer but lower amounts of NO_2 in the upper troposphere. This may reduce the AMF values (Eq. S4) because instrument sensitivity related SW is much higher in the upper troposphere than in the boundary layer and thus increases the total retrieval quantity. Unfortunately, there are no corresponding measurement data available to validate the CAMx and GEOS-Chem profiles in Fig. (S1), but similar bias has been found in the CAMx modeled NO_2 profile compared to the DC-8 and P-3 aircraft NO_2 measurements (Fig. 8). Using the CAMx profile here may introduce more errors to the OMI retrieval and inversions; hence, we do not recommend to either apply AK to the CAMx modeled VCD or to use the CAMx profile-based OMI in this study unless the CAMx profile is validated.

2. Impact of increased NO_x lifetime and artificial layer on modeled NO_2 VCD

The NASA OMI high resolution product used in this study shows reduced NO_2 in the rural areas, while enhanced NO_2 in the urban, compared to the NASA standard retrieval, version 2 (Tang et al., 2013); however, it still shows more smeared-out pattern than the CAMx modeled NO_2 VCD (Fig. S3a). The CAMx simulations with the a priori NO_x emission inventory created in Tang et al. (2013) shows larger NO_2 VCD in the cities, while lower NO_2 VCD in the rural places than OMI

(Fig. S3b). Reducing the reaction rate constant of the reaction OH + NO_2 by 25% in the CB05 chemical mechanism increases the NO_x lifetime, makes more NO_x transport to the rural, and enhances around 3% NO_2 VCD on average in the inversion region, but the impact is small (Fig. S3c). Implementing 40ppt NO_2 homogeneously into the model top layer adds about 1.6×10^{14} molecules.cm^{-1} NO_2 densities to each model grid and increases approximately 8% NO_2 VCD in the inversion region, further alleviating the NO_2 gap between OMI and CAMx in the rural areas (Fig. S3d).

3. Sensitivity of DKF inversion to error covariance matrices

The sensitivities of the DKF inversion-generated scaling factors to the uncertainties in the emission and observation error covariance matrices are tested for both region-based and sector-based DKF inversions to evaluate the robustness of the inversion results (Fig. S2). The OMI observation uncertainties are fixed to 30% in the sensitivity tests for the emission error covariance matrix, while the emission uncertainties are varied from 50% to 100% (Fig. S2 left). In contrast, the OMI observation uncertainties are varied from 10% to 50% in the sensitivity tests for the observation error covariance matrix, while the emission uncertainties in each sector are fixed to 100% (Fig. S2 right). In the region-based inversion, the emission uncertainties have insignificant impact on the inversion results. The inversion seems to be relatively responsive to the lower observation uncertainties, but results become more stable when the uncertainties are over 30% (Fig. S2 top). In the sector-based inversion, the scaling factors decrease when uncertainties in the observations increase, but the inversion results are less sensitive to the emission uncertainties. However, an exception occurs in the sector-based DKF inversion case I, where the adjustments in the aviation sector are relatively more sensitive to the emission uncertainty, ranging from 3.9 to 4.6 when emission uncertainty increases from 50% to 100%. It seems to offset against area and nonroad sector which the scaling factors reduce from 0.6 to 0.5 (Fig. S2 middle). However, the inversion becomes insensitive to the emission uncertainties in the sector-based DKF inversion case II when merging aviation into the area and nonroad sector (Fig. S2 bottom), indicating the DKF inversion in case II is more stable and less responsive to the uncertainty matrices than that in case I.

4. Top-down VOC emissions

Five VOC species, ethylene (ETH), ethane (ETHA), isoprene (ISOP), toluene (TOL), and xylene (XYL) are chosen to conduct the inversion in this study because of their explicit model outputs and sufficient measurement data. ETH, ISOP, TOL, and XYL are defined as highly reactive VOC (HRVOC) by TCEQ for regulatory purposes, due to their high reactivity with OH and propensity for contributing to rapid O_3 formation (Thomas et al., 2008). Although ETHA is not a HRVOC, the high concentrations in urban environments make it also play very important role in forming O_3 (Katzenstein et al., 2003; Buzcu and Fraser, 2006).

4.1 Base case VOC emission inventory

The base case VOC emission inventory for the HGB SIP modeling from 13 August to 15 September 2006 was developed by TCEQ (Table S1). The non-EGU point source VOC emissions were from the State of Texas Air Reporting System (STARS) database, a special inventory containing reported hourly VOC emissions from 15 August to 15 September targeting a specific list of non-EGU points and from Tank Landing Loss surveys of hourly landing loss VOC emissions. The EGU point source VOC emissions were from the EPA Acid Rain database (ARD) with the emissions calculated based on VOC:NO_x ratios. The VOC emissions from motor vehicle were generated by the Motor Vehicle Emission Simulator 2010a (MOVES2010a) model for the on-road vehicles and the Texas NONROAD (TexN) model for the off-road vehicles. The

VOC emissions from the other non-road and area sources were from the Texas Air Emissions Repository (TexAER) database (TCEQ 2010). The Global Biosphere Emissions and Interactions System model, version 3.1 (GloBEIS3.1) was used for developing biogenic VOC emissions (Yarwood et al., 1999). Four HRVOC species emissions, ethylene, propylene, 1,3-butadiene, and butenes were further corrected using the Potential Source Contribution Function (PSCF) technique with Automatic Gas Chromatographs (Auto-GC) measured data in the HGB area (TCEQ 2010).

For the five chosen VOC species, ETH and ISOP emissions are mostly contributed by the biogenic source around 60% and 99%, respectively, while TOL and XYL are entirely anthropogenic, originating mostly from area emissions. Area sources also dominate emissions of ETHA, which does not appear in the on-road mobile source. EGUs emissions are minor contributors to all five VOC species (Table S1).

4.2 VOC observations

The U.S. EPA Photochemical Assessment Monitoring Stations (PAMS) VOC measurement data (http://www.epa.gov/ttn/airs/airsaqs/) are used here to adjust emissions for the five chosen VOC species. All five VOC species were measured by the gas chromatographs-flame ionization detector (GC-FID) with 1-hr resolution for the entire modeling period from 13 August to 15 September 2006 in the unit of ppmC (U.S. EPA 1998). Measurements are available only for a total of 11 PAMS monitoring sites in the inversion region: 2 in DFW, 3 in BPA and 6 in HGB (Fig 1). The measurement data are first converted into the unit of ppb for each VOC species, and then averaged monthly over all monitoring sites in each region and compared to the corresponding modeled data.

The NOAA P-3 aircraft measured VOC data (http://www.esrl.noaa.gov/csd/tropchem/2006TexAQS/) are further used for evaluating the model performance in simulating aloft VOCs. Only four chosen VOC species, ETH, ISOP, TOL, and XYL are measured by P-3. ETH is measured using Laser Photoacoustic Spectroscopy (LPAS) with 20s resolution (de Gouw et al., 2009), and ISOP, TOL, and XYL are measured using Proton Transfer Reaction Mass Spectrometer (PTRMS) with 15s resolution (de Gouw et al., 2003). The P-3 measured ISOP, TOL, and XYL are available on 4 days (31 August, 11 September, 13 September, and 15 September 2006), while measured ETH is only available on 3 days (31 August, 13 September, and 15 September 2006) during our modeling period. The P-3 measured VOC data are averaged hourly and compared with the hourly modeled data at corresponding grid cells.

4.3 Results

Since all modeled ETH, ETHA, ISOP, TOL, and XYL are from the primary emissions, a direct scaling (DS) inversion method that adjusts VOC emissions based on the ratios between modeled VOC and PAMS measured VOC is applied here. The inversion is conducted on a regional basis, which means the scaling factor calculated from the measurement data in one region only applies to adjust the emissions in that region. Therefore, due to the availability of observations, the five chosen VOC species emissions are adjusted in only three regions, DFW, HGB, and BPA.

The scaling factors generated from the inversions vary significantly in different regions (Table S2) and show that the HRVOC emissions in the 2006 TCEQ emission inventory for HGB SIP modeling are much better than the reported uncertainty of an order of magnitude (Ryerson et al., 2003; Parrish et al., 2009) but still much higher than the uncertainty in NO_x emissions. The

ETHA emissions require the largest adjustments in all three regions with scaling factors ranging from 3.14 to 4.63. The inversion scales down ETH emissions in the HGB and DFW regions by only 10%, but in BPA, it requires a scaling factor of 3.33. The mostly biogenic source contributed ISOP emission only requires 4% scale-up adjustment in HGB, but relatively larger scale-down adjustments ranging from 30-50% in DFW and BPA. The anthropogenic source contributed TOL emissions require scale-up adjustments in all three regions by scaling factors ranging from 1.32 to 2.22. The XYL emissions are well estimated in the base case emission inventory for the HGB region, but require scale-down by approximately 70% in DFW and scale-up around 50% in BPA.

The temporal variations of the five VOC species (Fig.S4) show that the discrepancies between observed VOCs and the a priori modeled VOCs are significantly reduced by using the a posteriori emissions. The inverted ETHA emission improves modeled $R^2$and reduces modeled NMB and NME by 0.5 and 0.1, respectively (Table S3). The inversed ETH shows increased R^2 and 0.13 reduced NMB, but no improvement in the modeled NME against ground measurement (Table S3); however, it shows 0.4 reductions in both modeled NMB and NME against P-3 measured data (Table S4). The inverted ISOP emissions reduce approximately 20% NMB and NME in ground ISOP simulation (Table S3), but no improvements are found compared against aircraft measurement (Table S4). The modeled NMB in the inversed TOL is reduced by approximately 0.4 (Table S3) compared against PAMS and 0.13 compared against P-3 (Table S4), while the modeled NME has not been improved. The inversed XYL shows increased R^2 and around 0.2 reduced modeled NMB and NME compared to ground measurement (Table S3) and 0.02 reduced modeled NMB and NME compared to aircraft measurement (Table S4). However, no improvements are found in the model performance of simulating ground-level NO_2 (Table S5), and there is a slight decreasing, around 0.01, of modeled NMB and NME in ground-level O_3 simulations using the inverted VOC emissions (Table S6).

References

Boersma, K. F., Eskes, H. J., and Brinksma, E. J.: Error analysis for tropospheric NO_2 retrieval from space. J. Geophys. Res., 109, D04311, doi:10.1029/2003JD003962, 2004.

Bucsela, E. J., Krotkov, N. A., Celarier, E. A., Lamsal, L. N., Swartz, W. H., Bhartia, P. K., Boersma, K. F., Veefkind, J. P., Gleason, J. F., and Pickering, K. E.: A new stratospheric and tropospheric NO_2 retrieval algorithm for nadir-viewing satellite instruments: applications to OMI. Atmos. Meas. Tech., 6, 2607–2626, 2013.

Buzcu, B and Fraser, M. P.: Source identification and apportionment of volatile organic compounds in Houston, TX. Atmos. Environ., 40, 2385–2400, 2006.

de Gouw, J., Warneke, C., Karl, T., Eerdekens, G., van der Veen, C., and Fall, R.: Sensitivity and specificity of atmospheric trace gas detection by proton-transfer-reaction mass spectrometry. Int. J. Mass. Spectrom., 223– 224, 365–382, 2003.

de Gouw, J. A., Te Lintel Hekkert, S., Mellqvist, J., Warneke, C., Atlas, E. L., Fehsenfeld, F. C., Fried, A., Frost, G. J., Harren, F. J. M., Holloway, J. S., Lefer, B., Lueb, R., Meagher, J. F., Parrish, D. D., Patel, M., Pope, L., Richter, D., Rivera, C., Ryerson, T. B., Samuelsson, J.,Walega, J.,Washenfelder, R. A.,Weibring, P., and Zhu, X.: Airborne measurements of ethane from industrial sources using laser photo-acoustic spectroscopy. Environ. Sci. Technol., 43, 2437–2442, 2009.

Eskes, H. J. and Boersma, K. F.: Averaging kernels for DOAS total column satellite retrievals. Atmos. Chem. Phys., 3, 1285–1291, 2003.

Katzenstein, A. S., Doezema, L. A., Simpson, I. J., Blake, D. R., and Sherwood Rowland, F.: Extensive regional atmospheric hydrocarbon pollution in the southwestern United States. Proc Natl Acad Sci., 100, 11975–11979, 2003.

Martin, R. V., Jacob, D. J., Chance, K., Kurosu, T. P., Palmer, P. I., and Evans, M. J.: Global inventory of nitrogen oxide emissions constrained by space-based observations of NO_2 columns. J. Geophys. Res**.**, 108(D17), 4537, doi:10.1029/2003JD003453, 2003.

Parrish, D. D., Allen, D. T., Bates, T. S., Estes, M., Fehsenfeld, F. C., Feingold, G., Ferrare, R., Hardesty, R. M., Meagher, J. F., Nielsen-Gammon, J. W., Pierce, R. B., Ryserson, T. B., Seinfeld, J. H., and Williams, E. J.: Overview of the second Texas Air Quality Study (TexAQS II) and the Gulf of Mexico Atmosphere Composition and Climate Study (GoMACCS). J. Geophys. Res., 114, D00F13, doi: 10.1029/2009JD011842, 2009.

Ryerson, T. B., Trainer, M., Angevine, W. M., Brock, C. A., Dissly, R. W., Fehsenfeld, F. C., Frost, G. J., Goldan, P. D., Holloway, J. S., Hubler, G., Jakoubek, R. O., Kuster, W. C., Neuman, J. A., Nicks Jr., D. K., Parrish, D. D., Roberts, J. M., and Sueper, D. T.: Effect of petrochemical industrial emissions of reactive alkenes and NO_x on tropospheric ozone formation in Houston, Texas. J. Geophys. Res., 108 D084249, doi:10.1029/2002JD003070, 2003.

Tang, W., Cohan, D. S., Lamsal, L.N., Xiao, X., and Zhou, W.: Inverse modeling of Texas NO_x Emissions using space-based and ground-based NO_2 observations. Atmos. Chem. Phys., 13, 11005-11018, 2013.

TCEQ.: Houston-Galveston-Brazoria Attainment Demonstration SIP Revision for the 1997 Eight-Hour Ozone Standard, Austin, TX, 2010.
Thomas, R., Smith, J., Jones, M., MacKay, J., and Jarvie, J. Emissions Modeling of Specific Highly Reactive Volatile Organic Compounds (HRVOC) in the Houston-Galveston-Brazoria Ozone Nonattainment Area. TCEQ, Austin, TX, 2008.
U.S. EPA.: Technical Assistance Document for Sampling and Analysis of Ozone Precursors. U.S. EPA, Research Triangle Park, N.C. EPA/600-R-98/161., 1998.
Yarwood, G., Wilson, G., Emery C., and Guenther, A.: Development of the GloBEIS—a state of the science biogenic emissions modeling system. Final Report to the Texas Natural Resource Conservation Commission., Austin, TX., 1999.

Table S1. Emission rates of five VOC species for six emission sectors in the inversion region (tons/day).

VOCs	Area	On-road	Non-road	Biogenic	Non-EGU points	EGU points	Total
ETH	19.2 (11.5%)	14.9 (8.9%)	11.1 (6.6%)	104.8 (62.6%)	17.2 (10.3%)	0.1 (0.06%)	167.3
ETHA	232.4 (82.3%)	0 (0%)	5 (1.8%)	22.5 (8.0%)	20.4 (7.2%)	2.1 (0.7%)	282.4
ISOP	0.4 (0.002%)	0.8 (0.005%)	0.5 (0.003%)	15835.8 (99.9%)	0.2 (0.001%)	0 (0%)	15837.9
TOL	53.3 (48.9%)	24.5 (22.5%)	25.1 (23.1%)	0 (0%)	5.3 (4.9%)	0.7 (0.6%)	108.9
XYL	116.7 (58.3%)	38.2 (19.1%)	39.7 (19.8%)	0 (0%)	3.3 (1.6%)	2.2 (1.1%)	200.1

Note: percentage indicates the apportionment of each emission sector to the regional total.

Table S2. Direct scaling factors for VOC species in three inversion regions.

Source Region	A priori (tons/day)					Direct Scaling factors relative to a priori (unitless)				
	ETHA	ETH	ISOP	TOL	XYL	ETHA	ETH	ISOP	TOL	XYL
HGB	52.7	26.4	635.5	23.9	42.1	3.45	0.92	1.04	1.71	0.98
DFW	14.3	11.5	780.5	20.6	45.1	4.63	0.90	0.71	1.32	0.33
BPA	27.6	7.1	282.2	5.7	6.9	3.14	3.33	0.50	2.22	1.47

Table S3. Evaluation of CAMx modeled VOCs using hourly PAMS-measured VOCs.

Source Region	Priori					Posteriori				
	ETHA	ETH	ISOP	TOL	XYL	ETHA	ETH	ISOP	TOL	XYL
R^2	0.12	0.05	0.04	0.09	0.07	0.13	0.10	0.04	0.09	0.12
NMB	-0.71	-0.20	0.32	-0.41	0.24	-0.22	-0.07	0.05	-0.03	0.01
NME	0.73	0.80	1.04	0.63	0.90	0.61	0.81	0.86	0.69	0.69

Table S4. Evaluation of CAMx modeled VOCs using P-3 aircraft-measured VOCs[a].

Source Region	Priori				Posteriori			
	ETH[b]	ISOP	TOL	XYL[c]	ETH	ISOP	TOL	XYL
NMB	-0.63	-0.81	-0.60	-0.53	-0.59	-0.81	-0.47	-0.51
NME	0.84	1.05	0.72	0.80	0.80	1.05	0.72	0.78

a. Comparison available for four days (31 August, 11 September, 13 September, and 15 September 2006).
b. Comparison only available for three days (31 August, 13 September, and 15 September 2006).
c. Compared with measured C-8 aromatics

Table S5. Evaluation of CAMx modeled NO_2 using hourly AQS ground-measured NO_2.

Source Region	Priori			Posteriori		
	R^2	NMB	NME	R^2	NMB	NME
HGB	0.51	0.46	0.67	0.51	0.46	0.67
DFW	0.49	0.43	0.66	0.49	0.43	0.66
BPA	0.45	0.92	1.02	0.45	0.92	1.02
Overall	0.51	0.51	0.72	0.51	0.51	0.73

Table S6. Evaluation of CAMx modeled O_3 using hourly AQS ground-measured O_3.

Source Region	Priori			Posteriori		
	R^2	NMB	NME	R^2	NMB	NME
HGB	0.46	0.68	0.75	0.46	0.68	0.75
DFW	0.64	0.21	0.32	0.64	0.20	0.31
BPA	0.47	0.66	0.70	0.46	0.65	0.69
Overall	0.50	0.42	0.50	0.50	0.41	0.49

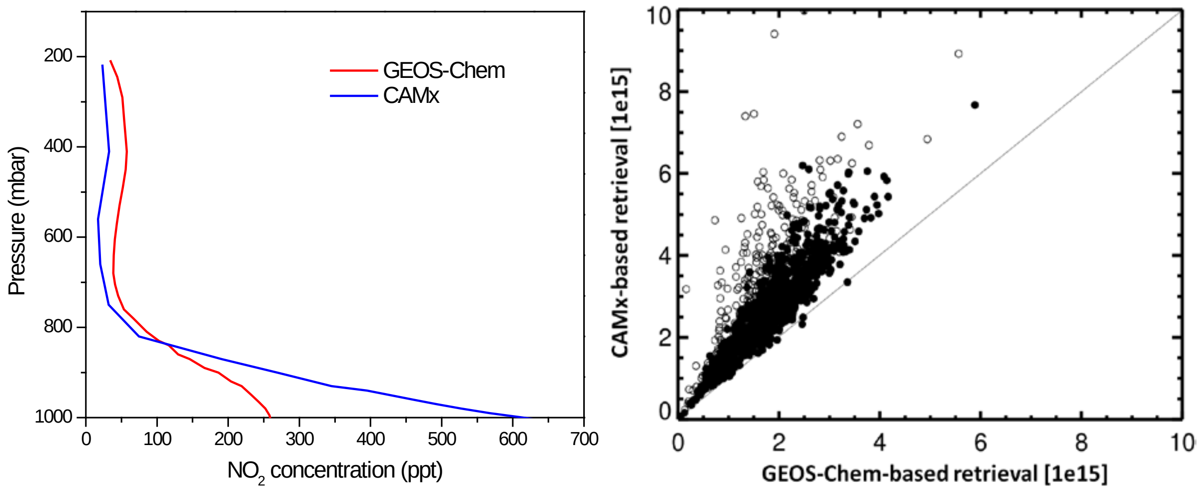

Figure S1. Comparisons between GEOS-Chem and CAMx modeled NO_2 vertical profiles (left) and corresponded OMI retrievals (right). Filled circles represent observations under clear sky condition (cloud fraction <0.5), and open circles are all observations.

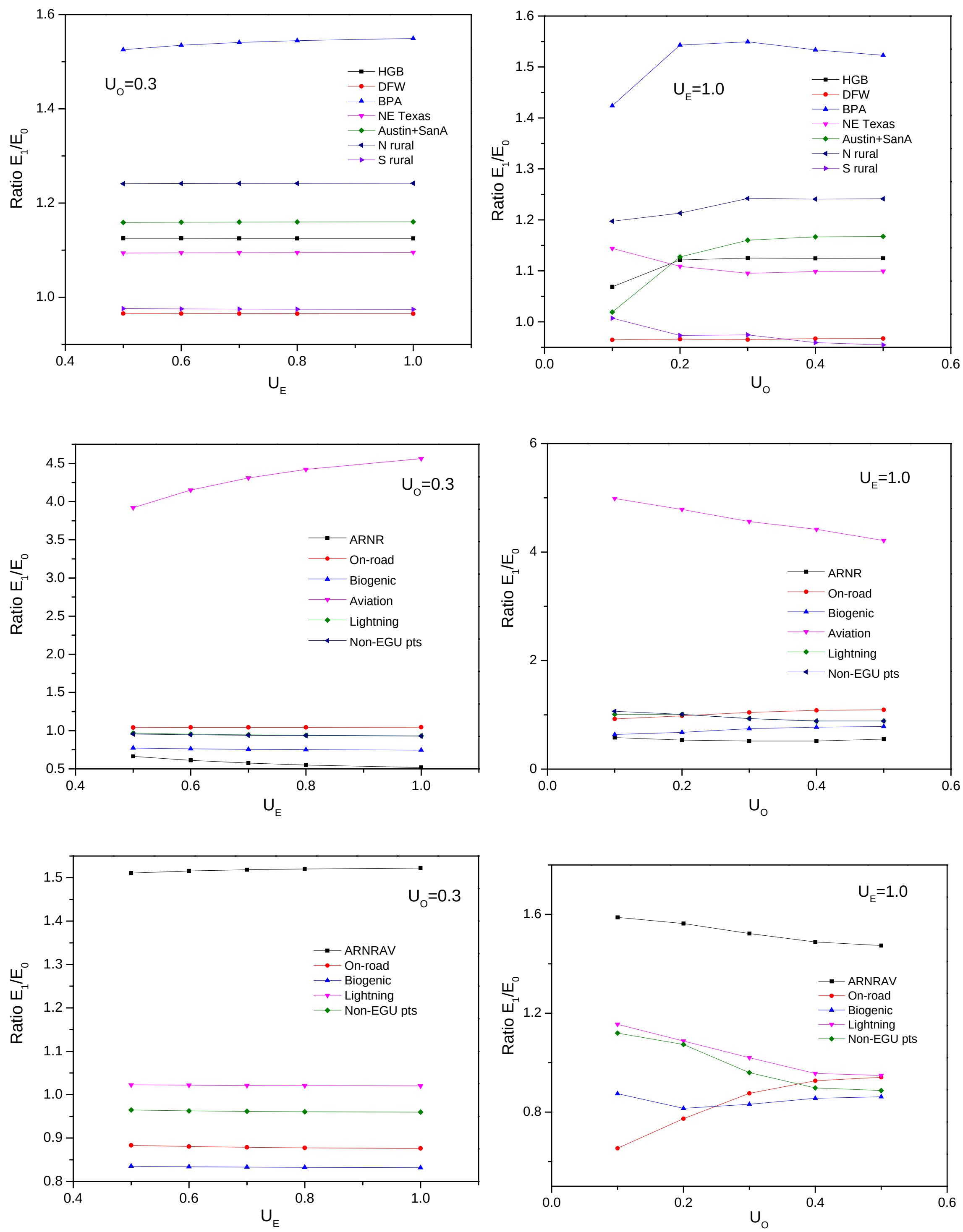

Figure S2. Sensitivities of the DKF inversions to the uncertainties in emissions (left) and in OMI observations (right) in region-based inversion (top), sector-based inversion case I (middle), and sector-based inversion case II (bottom).

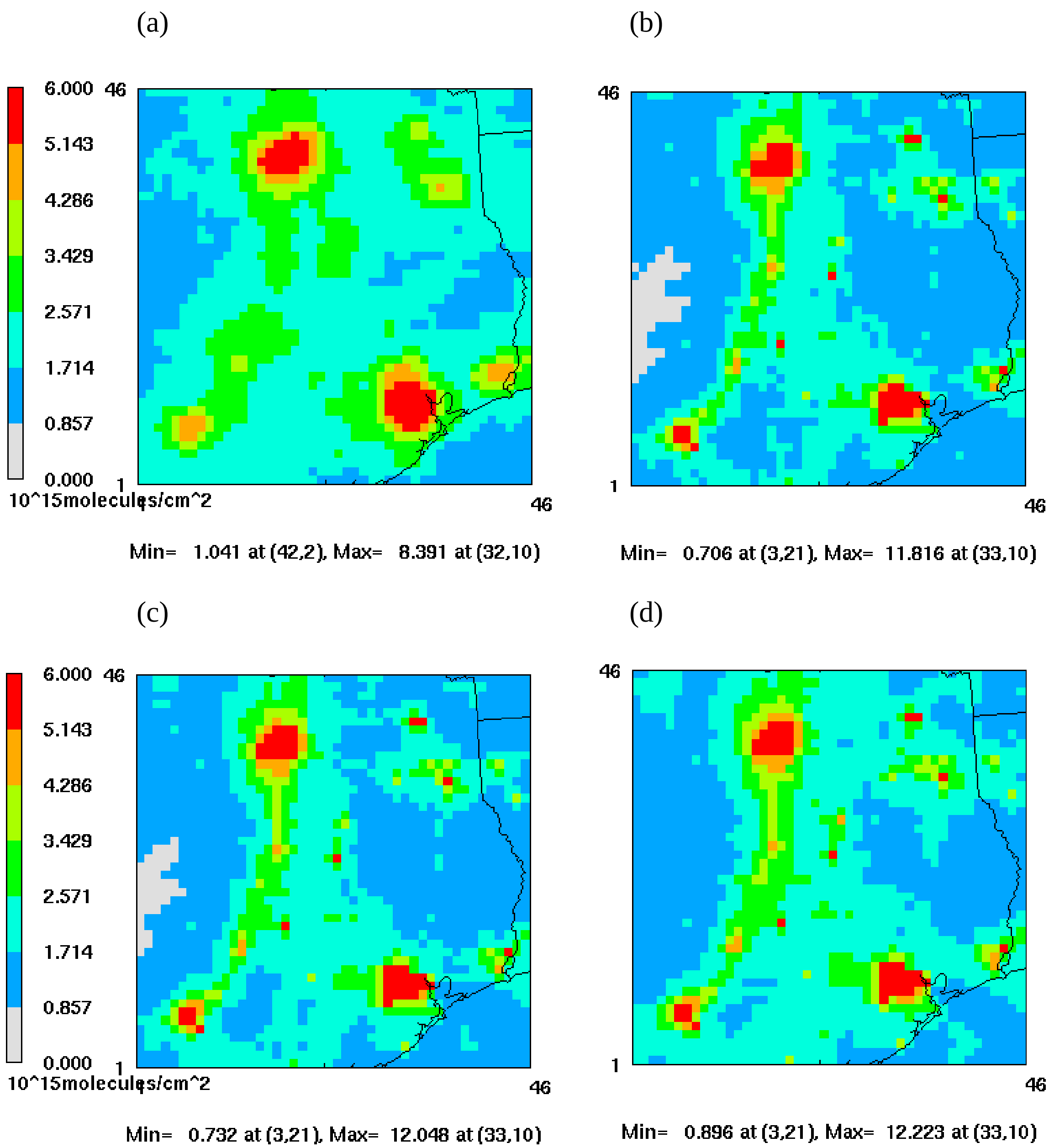

Figure S3. Monthly averaged (16 August to 15 September) tropospheric NO_2 VCDs at 13:00-14:00LT from (a) OMI, (b) simulations using NO_x emissions from Tang et al., (2013), (c) simulations with the lower rate constant of the reaction $OH+NO_2$ from (b), and (d) simulations with added 40ppt NO_2 layer from (c).

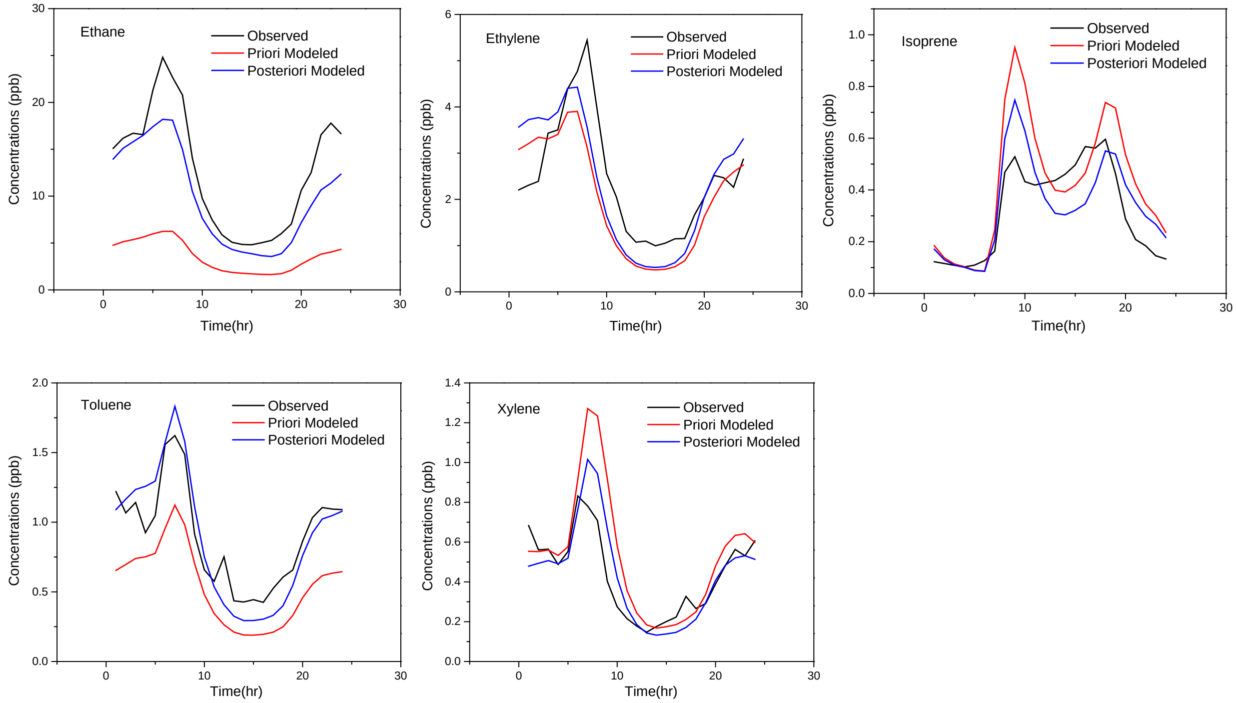

Figure S4. Comparisons of monthly averaged daily variation between observed (black) and modeled VOC species using the a priori (red) and the a posteriori (blue) VOC emission inventory over all monitoring sites.